Redondo-Cubero, A., Lorenz, K., Palomares, F. J., Muñoz, A., Castro, M., Muñoz-García, J., Cuerno, R. y Vázquez, L. (2018). Concurrent segregation and erosion effects in medium-energy iron beam patterning of silicon surfaces. *Journal of Physics Condensed Matter*, 30(27).

DOI: https://doi.org/10.1088/1361-648X/aac79a

Concurrent segregation and erosion effects in medium-energy iron beam patterning of silicon surfaces

A Redondo-Cubero[1], K Lorenz[2], F J Palomares[3], A Muñoz[4], M Castro[5,6], J Muñoz-García[7], R Cuerno[7], and L Vázquez[3]*

[1] Electronics and Semiconductors Group, Departamento de Física Aplicada, Universidad Autónoma de Madrid, 28049 Madrid, Spain

[2] INESC-MN, IPFN, CTN, Instituto Superior Técnico, Universidade de Lisboa, 2695-066 Bobadela LRS, Portugal

[3] Instituto de Ciencia de Materiales de Madrid (CSIC), 28049, Madrid, Spain

[4] Departamento de Física, Universidad Carlos III de Madrid, 28911 Leganés, Spain

[5] Grupo Interdisciplinar de Sistemas Complejos (GISC) and Grupo de Dinámica No Lineal (DNL), Escuela Técnica Superior de Ingeniería (ICAI), Universidad Pontificia Comillas, 28015 Madrid, Spain

[6] School of Mathematics, University of Leeds, UK

[7] Departamento de Matemáticas and GISC, Universidad Carlos III de Madrid, 28911 Leganés, Spain

E-mail: `lvb@icmm.csic.es (corresponding author)`

Abstract. We have bombarded crystalline silicon targets with a 40 keV Fe^+ ion beam at different incidence angles. The resulting surfaces have been characterized by Atomic Force, Current-sensing and Magnetic Force Microscopies, Scanning Electron Microscopy, and X-ray Photoelectron Spectroscopy. We have found that there is a threshold angle smaller than 40° for the formation of ripple patterns, which is definitely lower than those frequently reported for noble gas ion beams. We compare our observations with estimates of the value of the critical angle and of additional basic properties of the patterning process, which are based on a continuum model whose parameters are obtained from binary collision simulations. We have further studied experimentally the ripple structures and measured how the surface slopes change with the ion incidence angle. We explore in particular detail the fluence dependence of the pattern for an incidence angle value (40°) close to threshold. Initially, rimmed holes appear randomly scattered on the surface, which evolve into large, bug-like structures. Further increasing the ion fluence induces a smooth, rippled background morphology. By means of microscopy techniques, a correlation between the morphology of these structures and their metal content can be unambiguously established.

1. Introduction

Ion-beam sputtering (IBS) induced patterning of surfaces has been intensively studied both experimentally and theoretically in the last years [1, 2]. This technique is able to produce ripple or dot nanopatterns on many surfaces, with silicon being one of the most extensively studied systems [2], due to its monoelemental nature, flatness, and widespread availability. Precisely, the studies performed on Si surfaces have allowed to elucidate the key role played by the (some times, unintended) simultaneous metal supply during noble gas irradiation [3]. The scenario of IBS patterning has become thus clarified and is now clearly divided into two main groups of studies. The first group focuses on noble gas IBS without any simultaneous metal supply [4, 5, 6]. The second group corresponds to the case in which impurity deposition takes place concurrently with IBS; in many cases, the noble gas ion beam impinges simultaneously on the Si surface and on an adjacent metal (usually Fe-rich) plate [7, 8, 9, 10]. In this way, the metallic atoms that are sputtered from the plate eventually land on the Si target surface leading to silicide formation. The silicide-rich regions finally protrude under IBS because of their lower sputtering yield, which results into a morphological instability and pattern formation [9, 10]. Such a metal-assisted IBS process, although usually leading to more complex behaviors, has been also studied theoretically [11, 12, 13, 14]. Most of the experimental studies have been made with the adjacent metal plate set-up described above, both at low [7, 8, 9, 10, 15, 16] and at medium [17, 18] ion energies. With this set-up, the incoming ions and the metal supply follow different paths and land on the target surface at different angles.

In contrast, very few works have dealt with IBS pattern formation on Si surfaces when they are bombarded with a metal ion beam [19, 20, 21], where both the ion beam and the metal supply follow the same path and impinge on the Si surface under the same angle. While in [19] an Au^- beam was employed, less likely leading to silicide formation, in [20, 21] a 5 keV Fe^+ beam was employed under an oblique incidence angle of 65°. In the latter studies, ripple morphologies were obtained and the residual stress distribution was addressed in order to characterize the depth profile of the ensuing iron silicide. Compound-forming systems undoubtedly show more complex pattern formation and development than impurity-free cases. Nevertheless, it is still interesting to identify in them dynamical surface behavior that has been well stablished for the case of noble gas IBS without metal incorporation [3, 4, 22]. Particularly interesting issues include the existence of a threshold incidence angle for surface patterning and the potential correlations between the Fe content and the surface morphology. These issues have not been fully addressed yet, specially at medium ion energies.

The aim of the present work is to further explore the morphological behavior of Si surfaces irradiated with a medium-energy Fe^+ beam at different incidence angles ϑ. Special attention will be paid to the time evolution of the induced morphology for a fixed angle $\vartheta = 40°$, which is close to the threshold value. At this incidence condition, peculiar bug-like microstructures appear which will be analyzed in detail. Whenever possible,

we have carried out systematic morphological characterizations, similar to those already reported for noble gas IBS of Si surfaces without metal supply, in order to be able to compare both types of systems. In particular, we present an estimate for the value of the critical angle which is based on a continuum model of impurity-free amorphizable targets, whose parameters are obtained from Monte Carlo simulations within the binary collision approximation.

2. Methods

The implantation experiments were performed at room temperature with a 20 keV or 40 keV Fe^+ beam extracted from a Danfysik 1090 ion implanter with a base pressure of $5{\times}10^{-6}$ mbar. The ions impinged on the single-crystal Si(100) targets ($1{\times}$ 1 cm^2) at different angles (from 0° up to 70°) with respect to the surface normal and a total fluence of 10^{18} ions/cm^2 with a current density of 18 μA cm^{-2} in the sample plane. To obtain homogeneous irradiation, the focused beam was scanned with a magnetic x-y sweeping system. In addition, to avoid any unwanted metal supply from the surrounding sample holder plate, the sample was placed on top of a 10 mm high cylinder with 10 mm diameter. For the samples irradiated at 40° the initial stages of the irradiation were analyzed under increasing fluence, from 10^{17} up to 10^{18} ions/cm^2.

The resulting surface morphology was imaged ex-situ by AFM operating in the dynamic mode with Nanoscope IIIa equipment (Bruker©) and with an Agilent PicoPlus 5500, the latter being able to operate in the current or magnetic sensing modes. The current sensing imaging was performed in an environmental chamber in which nitrogen gas was fed in, to drastically decrease the humidity. Silicon cantilevers with a nominal radius of 8 nm and force constant of 40 N/m (Bruker) were employed for the topographical measurements. For the MFM measurements CoCr coated cantilevers (Bruker) with a nominal radius of 35 nm and force constant of 75 N/m, were employed. For the Cs-AFM measurements, diamond coated (CDT-FMR, $r \sim 83 \pm 17$ nm from NanoWorld, and DCP11, $r \sim 60 \pm 10$ nm from NT-MDT) tips were employed and tip-sample biases of $2-6$ V were used.

We have analyzed statistically the AFM images in order to describe the induced surface morphology. Thus, denoting by $h(\mathbf{r})$ the value of the surface height above point $\mathbf{r}$ on the substrate plane, we have computed the surface roughness $\sigma = \left(\sum_{\mathbf{r}} \left[h(\mathbf{r}) - \bar{h}\right]^2 / L^2\right)^{1/2}$, where $\bar{h}$ is the space average of the measured heights, as obtained from AFM images of size L, using the software of the equipment. Likewise, the height skewness, which measures the lack of up-down symmetry of the height distribution around its mean [23], has been evaluated with the same software as $\gamma_1 = \sum_{\mathbf{r}} \left[h(\mathbf{r}) - \bar{h}\right]^3 / (L^2\sigma^3)$. Further image analysis has been carried out using the Gwyddion freeware package [24]. In particular, we have obtained the power spectral density (PSD), defined as

$$\mathrm{PSD}(\mathbf{k}) = \langle |h(\mathbf{k})|^2 \rangle, \tag{1}$$

where the brackets denote statistical average and $h(\mathbf{k})$ is the 2D (space) Fourier transform of the surface height $h(\mathbf{r})$ [23]. We have also computed a final important function, namely, the height autocorrelation function [25, 24] (ACF),

$$\mathrm{ACF}(\mathbf{r}) = \langle h(\mathbf{r}_0)h(\mathbf{r}_0+\mathbf{r})\rangle. \tag{2}$$

SEM images were obtained with a Field-emission Scanning Microscope, TENEO equipment (©FEI) operating with a 5 keV electron beam and a current in the range of 0.2-0.4 nA. Concentric backscattered detector (CBS) and Everhart-Thornley through-lens detector (ETD) for secondary electrons were simultaneously used.

Chemical analysis of the samples was also carried out, through a high-resolution XPS system using monochromatic Al Kα radiation and a SPECS Phoibos 150 hemispherical spectrometer. The spectra were recorded at normal emission take-off angle, using an energy step of 0.05 eV and a pass-energy of 10 eV, which provides an overall energy resolution of approximately 0.40 eV.

3. Results and Discussion

Figure 1 displays characteristic morphologies induced on the silicon surface after 40 keV Fe^+ ion bombardment with an ion fluence of 10^{18} ions/cm^2, for different incidence angles. Additionally, Figures 2 and 3a show, respectively, the 1D PSD along the ion-beam direction (x-axis) and the surface roughness and skewness values. For $\vartheta = 15°$, a smooth, featureless morphology is obtained with $\sigma = 0.3$ nm, a slightly larger roughness than that of the raw silicon surface. At 30°, the surface still remains smooth ($\sigma = 0.8$ nm) but a clear granular morphology has developed with a typical grain size in the $70-110$ nm range. However, the surface morphology changes abruptly upon increasing the incidence angle up to 40°, since bug-like structures [9] are found scattered over a homogeneously rippled surface. The ripples, which run perpendicular to the ion-beam direction, have amplitudes from just 3 nm up to 10 nm, and a typical wavelength $\lambda \simeq 390$ nm. All the bug structures look quite similar, mostly presenting an elliptical shape whose long axis (around 2.8 μm) is perpendicular to the ion-beam direction and to the short axis (1.7 μm). Interestingly, bug structures display smaller replicas at their tails, as seen by the ion beam. The protrusion of the bug structures over the rippled background leads to a considerable roughness increase up to $\sigma = 22$ nm, as well as to a large positive value of the skewness.

By increasing the ion-beam angle up to $\vartheta = 50°$, the surface morphology changes again sharply. Now, a rippled-like morphology is observed. The ripples or stripes run also perpendicular to the ion beam and have a wavelength $\lambda = 250 - 280$ nm. The homogeneity of the morphology reflects into a drop of the skewness, whereas the roughness reaches its maximum value, $\sigma \simeq 25$ nm. When the ion-beam angle is set at 60° the resulting morphology is akin to that obtained at 50°, with strip structures running perpendicular to the ion-beam direction. However, the morphology seems more disordered in the vertical direction. At this condition the roughness has decreased

slightly ($\sigma \simeq 22$ nm) and the skewness is still low. Finally, at $\vartheta = 70°$, the surface displays a sort of terraced structure running parallel to the ion-beam direction.

In order to assess the lateral ordering of the induced nanostructures, a useful tool is the ACF function, equation (2), taking $\mathbf{r}$ along the x or the y axes, defining ACF_x and ACF_y, respectively. In figure 1 these data are shown below the AFM image for each system. For small angles, $\vartheta = 15°$ and $\vartheta = 30°$, no clear oscillation is detected in the ACFs, indicating the absence of nanostructure ordering. However, for $\vartheta = 40°$ a clear oscillation is observed in ACF_x that is not present in ACF_y. Such an oscillating behavior is due to the ripple morphology, its average period corresponding to the ripple wavelength [25]. For even larger incidence angles, the oscillations become less clear, due to the roughening of the surface, which disorders the lateral distance between neighboring nanostructures. In any case, more oscillations are seen along the x than along the y direction, indicating some preferential arrangement. This behavior changes finally at $\vartheta = 70°$, when more clear oscillations occur along the y-axis, indicating that the pattern has rotated its orientation by 90°.

Further information on the pattern morphology can be obtained from the surface PSD along the ion-beam direction (x-axis). These curves are shown in figure 2 for those angles for which a pattern is observed. Clearly, the curves are quite complex. Roughly, below $\vartheta = 70°$ the PSDs show a linear region for large k values (i.e., short distances) with a high slope of -4.6 to finally reach a k-independent behavior for small k. The crossover between the small- and large-k regions, marked by vertical arrows, indicates the average wavelength of the rippled structures. This behavior indicates that the global surface roughness is mainly defined by the ripple morphology [26]. In contrast, for $\vartheta = 40°$ the saturation value in the PSD is determined by the large bug structures: indeed, the wavelength associated with the smaller ripple morphology is not even detected in the PSD, its contribution to the surface roughness being overcome by that of the large bugs. This is confirmed by the dashed curve in figure 2, which shows the PSD corresponding to a rippled region without any bug. Now a clear peak appears, whose k value corresponds to the average ripple wavelength. The interpretation of the PSD for $\vartheta = 70°$ is more complex, as the pattern is different. It is worth mentioning that a peak appears in the PSD along the y-axis (not shown), in contrast to its absence in figure 2, consistent with the fact that the pattern has rotated by 90° as seen in the ACF plots. Finally, the large slope of the linear region at large k indicates that a strong morphological instability is taking place at scales smaller than the ripple structure.

The geometry of the ripple/strip morphologies can be analyzed using the formalism employed by Engler et al. [5] for the case of silicon irradiated with an oblique 2 keV Kr^+ ion beam. The different angles describing the system geometry in this work are defined in the inset of Figure 3b. Thus, with ϑ being the angle of the ion beam with respect to the unirradiated target normal, the sides along the projection of the ion-beam direction are termed as upwind/downwind as they do/do not face the incoming ion beam. On each side two angles are defined: the local slope (α_u, α_d) and the local incidence angles (θ_u, θ_d). We have followed the same procedure established in [5] to obtain the values

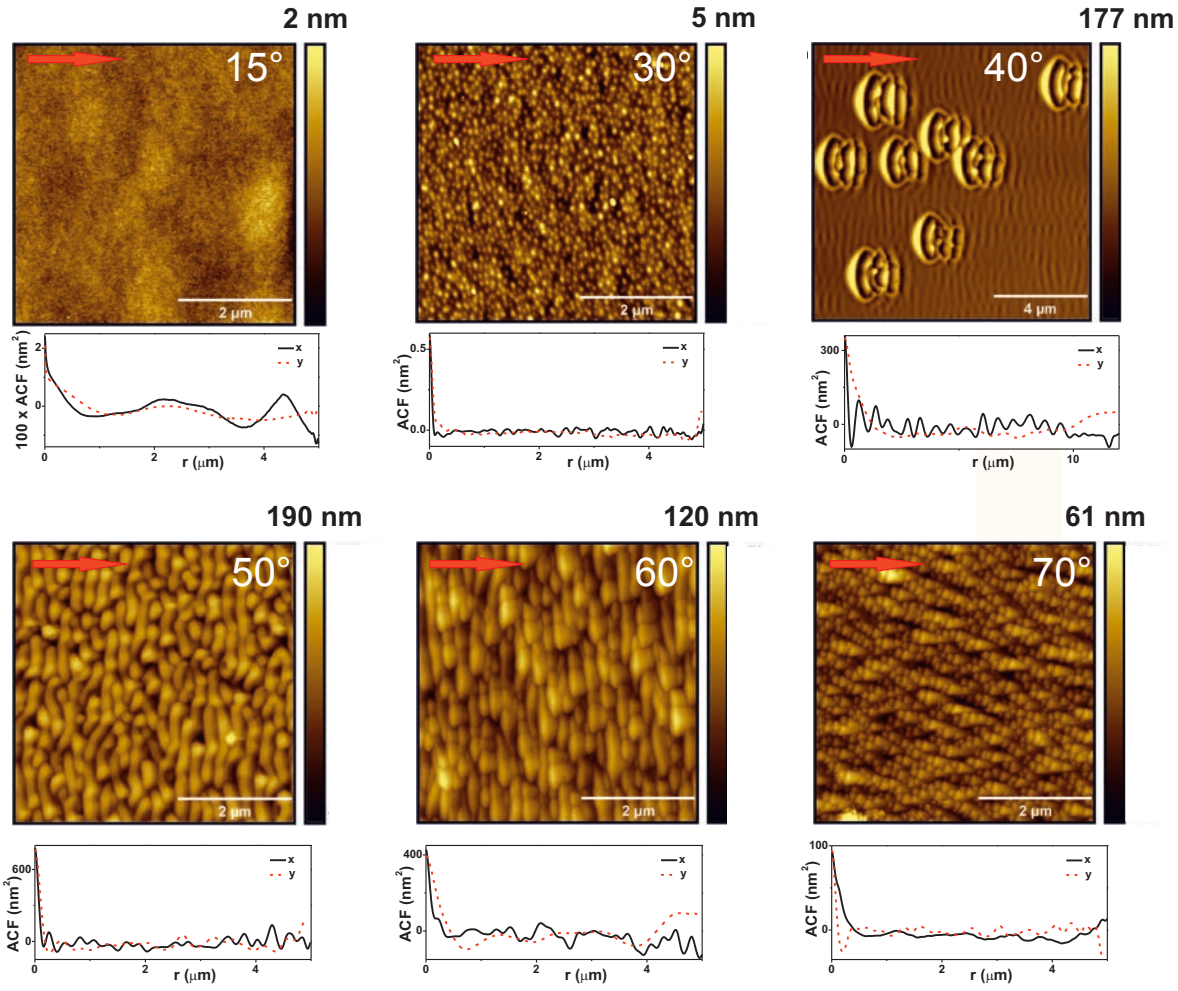

Figure 1. AFM images of the surface morphology induced on a silicon surface after 40 keV Fe^+ ion irradiation with a fluence of 10^{18} ions/cm^2 at different incidence angles with respect to the unirradiated surface normal, as indicated in each image. The ion-beam direction is from left to right, as indicated by the red arrows. For each case, the ACF obtained along the x (solid black line) and y (dashed red line) directions are shown below the corresponding AFM top-view.

of α and θ. In Figure 3b we plot the change of θ_u and θ_d with the ion-beam incidence angle ϑ. We can compare the values of θ_u and θ_d for $\vartheta = 60°$ and $\vartheta = 70°$ with those reported by Khanbabaee [20] for 5 keV Fe^+ ions impinging at $\vartheta = 65°$. In our case, θ_u is higher than 33°, which is the value observed in [20], while θ_d is a few degrees higher. The behavior observed for our two incidence angles is different from that observed for the Kr^+/Si system for ion-beam angles in the $55° - 80°$ range. Specifically, in our case θ_u increases at a larger rate than ϑ whereas in the Kr^+/Si system θ_u fluctuated slightly around 50°. Furthermore, in our system $\theta_d \simeq 78°$ essentially remains constant. In contrast, in the Kr^+/Si system θ_d increased monotonically with ϑ, with a fixed 8° shift. Thus, our system differs from the Kr^+/Si case, which can be due both to the ion energy employed (8 times larger in our case) and, most likely, to the chemical reaction between

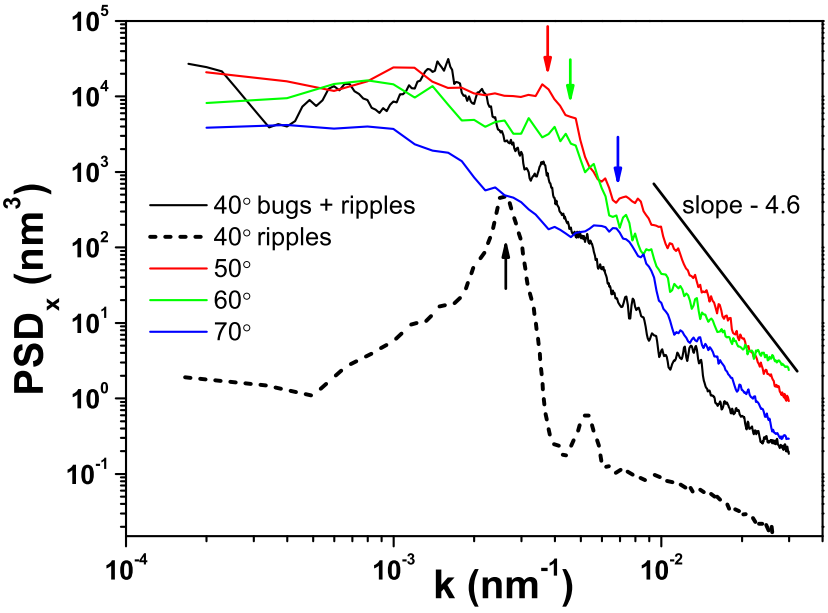

Figure 2. Logarithmic plot of the PSD functions obtained along the x-axis for the samples irradiated under an angle of $\vartheta = 40°$ or larger. For $\vartheta = 40°$ case the PSD is also shown for a rippled region without any bug (dashed curve). The vertical arrows mark the k-values corresponding to the average ripple wavelength for each case (each arrow corresponds to the curve of the same color). The straight line for large k values corresponds to power-law behavior as $\mathrm{PSD}_x \sim k^{-4.6}$.

the incoming Fe ions and the Si substrate leading to silicide formation. This has the additional effect of changing the local sputtering yield [9, 27, 28]. It is worth noting that shadowing effects [29] are not detected in any of these systems since they would lead to $\theta_d \simeq 90°$ values, which is not the case despite the large incidence angles employed.

From the data shown in Figure 1, it is clear that a non-zero threshold angle for ripple formation, ϑ_c, exists in our present system, with $30° < \vartheta_c < 40°$. This value is clearly smaller than those reported on impurity-free Si irradiated with low energy noble gas ions [2, 3, 4, 22]. Furthermore, our ϑ_c value is also smaller than the few reported threshold angles found in silicon under medium-energy noble gas ion-beam irradiation [30, 31, 32]. In all these cases, the threshold angle was 45° or higher.

The value of ϑ_c may be affected by experimental uncertainties in the ion-beam angle and by the beam divergence. In order to characterize it further, we have made three additional experiments at the same fixed fluence, 10^{18} ions/cm^2, for 20 keV Fe^+ ions impinging at $\vartheta = 15°$, 30°, and 40°. Representative AFM images are displayed in Figures 3d-f. At $\vartheta = 15°$, a smooth, mainly featureless surface is observed (note the vertical scale of just 2 nm). In contrast, at $\vartheta = 30°$ and $\vartheta = 40°$ the overall morphology shows structures scattered on the flat surface, akin to the initial stages of formation of the bug structures observed at 40 keV. Furthermore, the insets show details of this flat area, where incipent ripples can be observed, with a tendency to arrange along the ion-beam direction. For $\vartheta = 30°$ the ripples have a rather small amplitude around 0.5

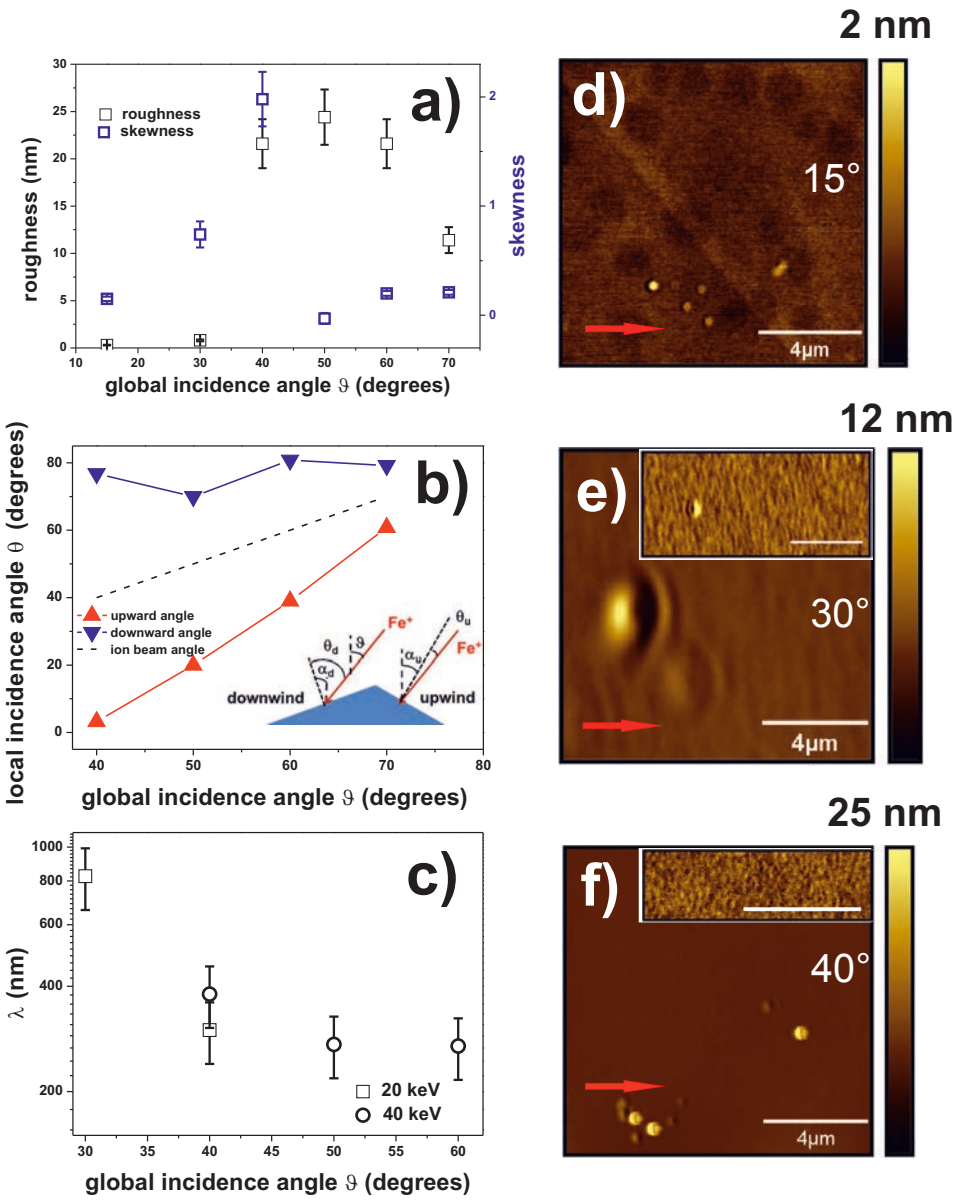

Figure 3. (a) Surface roughness (black filled squares, left y-axis) and skewness (open blue squares, right y-axis) vs ion-beam incidence angle. (b) Plot of θ_u and θ_d vs ion-beam incidence angle. Inset: Scheme showing the ripple and ion-beam irradiation geometry with the definitions of ion-beam incidence angle (ϑ), the upwind and downwind ripple sides, the local slopes (α_u and α_d), and the local incidence angles (θ_u and θ_d). (c) Ripple wavelength vs ion-beam incidence angle for 20 keV (filled squares) and 40 keV (open circles) Fe^+ ions at 10^{18} ions/cm^2 fluence. d-f) AFM images of the surface morphology induced on a silicon surface after 20 keV Fe^+ ion irradiation with a fluence of 10^{18} ions/cm^2 at different incidence angles with respect to the unirradiated surface normal, as indicated in each image. The ion-beam direction is from left to right, as indicated by the red arrows. For the two largest angle values, the insets show a detail of the ripple morphology. The horizontal bar corresponds to 10 μm (5 μm) for $\vartheta = 30°$ (40°).

nm, and very large wavelength, $\lambda \simeq 0.83$ μm, whereas at $\vartheta = 40^\circ$ ripples also exist but with a smaller wavelength. Figure 3c displays the change of the ripple wavelength with incidence angle for 20 keV and 40 keV. In both cases, λ decreases with ϑ in agreement with other experimental reports in which noble gas ions were employed, both at low [4, 22] and at medium [31] energies. Also, as ϑ approaches ϑ_c, λ increases abruptly, as occurs for noble gas IBS of Si [4, 22], and as predicted by a model that is based on stress-induced viscous flow in the ion-amorphized topmost surface layer [4]. We should remark, however, that ion reaction with the silicon target atoms is not contemplated in this model, but see below. Finally, ϑ_c increases with ion energy, perhaps related with the different stress distribution throughout such an amorphized layer.

3.1. Morphological instability

Drawing upon current theoretical knowledge of the IBS process at low energy, it is possible to approximately account for some of the basic properties of the patterning process in our present context, namely, the occurrence of a non-zero critical angle ϑ_c and the rotation of the pattern at high angles of incidence. Both can be in principle described within a linear continuum model [1, 2] of the form

$$\frac{1}{J}\frac{\partial h}{\partial t} = C_{11}\frac{\partial^2 h}{\partial x^2} + C_{22}\frac{\partial^2 h}{\partial y^2} - \mathcal{K}\nabla^4 h, \tag{3}$$

where $h(x, y, t)$ is the surface height at time t above point (x, y) on the target plane –with the x-axis lying along the projection of the ion-beam direction– and J is the ion flux. Patterns form under conditions (e.g. $\vartheta > \vartheta_c$) such that C_{11} or $C_{22} < 0$. For $\vartheta \neq 0$, patterns are anisotropic and rippled, being periodic along the direction, x or y, which features the most negative C_{ii} coefficient [1, 2]. Different physical mechanisms induce dependencies of the coefficients $C_{11,22}$ and $\mathcal{K}$ on different experimental parameters like incidence angle, etc., but do not modify the structure of the equation of motion sufficiently close to pattern onset.

We consider three basic mechanisms that have proved to have a large explanatory power for IBS of semiconductor targets, for irradiation conditions dominated by nuclear stopping [2], as in our present case: first, the unstable curvature dependence of the sputtering yield, as recently modeled in [33, 34]; second, mass-redistribution induced at the target surface by the collision cascades [35, 36, 37] [the so-called Carter-Vishnyakov (CV) effect, possibly related at a mesoscopic level with the ion-induced viscous flow model [4] mentioned above], and ion implantation [14]. Building upon a linear superposition principle in equation (3), we expect each physical mechanism to independently contribute to the height equation of motion, leading to

$$C_{ii} = C_{ii}^{\mathrm{sputt}} + C_{ii}^{\mathrm{CV}} + C_{ii}^{\mathrm{impl}}, \quad i = 1, 2, \tag{4}$$

where the coefficients on the right-hand side can be analytically computed [33, 34, 35, 36, 37, 14]. Among the terms in equation (3), we focus on the contributions to the second order derivatives, since they control the morphological stability of the system. The

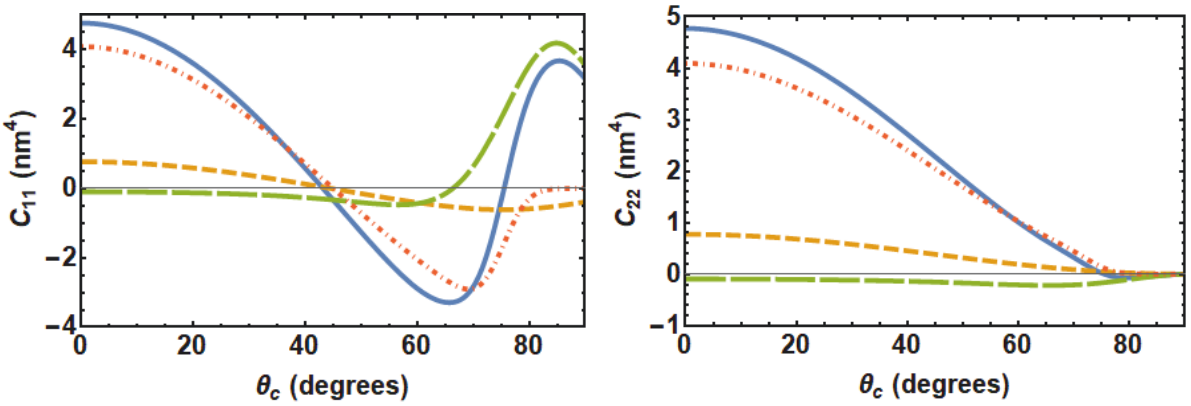

Figure 4. Incidence-angle dependence of coefficients C_{11} (left panel) and C_{22} (right panel) in (3) (solid blue lines), using parameters for 40 keV Fe^+ irradiation of Si as estimated by SRIM, see the Appendix. On each panel, the contributions due to each single mechanism as in (4) are shown as long-dashed, green lines ($C_{ii}^{\rm sputt}$), dotted-dashed, red lines ($C_{ii}^{\rm CV}$), and short-dashed, brown lines ($C_{ii}^{\rm impl}$), respectively.

analytical expressions for $C_{11,22}^{\rm sputt,CV,impl}$ turn out to depend explicitly in the ion incidence angle, as well as on additional parameters like ion penetration depth, lateral stragglings, etc. which can be numerically estimated by Monte Carlo simulations within a binary collision approximation employing SRIM [38]. To this end, we follow the procedure described in detail in [39] for the case of 1 MeV Au^+ irradiation of Ti-related targets. For our case of Fe^+ irradiation of Si, this procedure leads to the parameter values reported in Table A1 in the Appendix. Using those values, we can already get insight into the relative importance of each of the physical mechanisms considered in equation (4) through the following order-of-magnitude estimates [39]: $C_{11}^{\rm sputt} \approx \Omega_{\rm Si} Y(0) a_{\rm sputt} = 0.54$ nm^4 [33, 34], $C_{11}^{\rm CV} \approx \Omega_{\rm Si}\delta = 4.09$ nm^4 [35, 36, 37], and $C_{11}^{\rm impl} \approx \Omega_{\rm Si}\alpha_{\rm impl}\beta_{\rm impl}/a_{\rm impl} = 0.10$ nm^4 [14]. Here, $Y(0)$ is the average sputtering yield at normal incidence, $\Omega_{\rm Si}$ is the atomic volume of Si, a, α, and β are the average deposition depth, the longitudinal, and the transverse stragglings for sputtering (sputt) or implantation (impl), and δ is the average travel distance of recoil atoms. According to these estimates, mass redistribution seems to dominate the dynamics of the target surface.

Actually, the full incidence angle dependence of all the coefficients appearing in equation (4) can be obtained in detail; results are provided in figure 4. Indeed, the dominant contribution to C_{11} and C_{22} is mass redistribution, for all incidence angles up to roughly $\vartheta = 70°$, above which sputtering takes over as the most significant contribution. Ion implantation actually dominates over sputtering approximately up to that angle too. As both coefficients $C_{11}, C_{22} > 0$ for incidence angles $\vartheta < \vartheta_{c,theor}$, while C_{11} changes sign at $\vartheta = \vartheta_{c,theor}$, the results in figure 4 predict a critical angle value $\vartheta_{c,theor} \simeq 43°$, not very far off the experimental estimate. Note, C_{22} remains positive up to high incidence angles, hence the ensuing ripple structure is predicted to be periodic along the x direction, as observed, for angles $\vartheta_{c,theor} < \vartheta < \vartheta_*$. Here, $\vartheta_* \simeq 76°$ is the

angle above which C_{22} becomes more negative than C_{11}; hence, the present linear model predicts a rotation of the ripple structure by 90 degrees at $\vartheta = \vartheta_*$. In our experiments, a rotated pattern is already seen for $\vartheta = 70°$, recall figure 1.

Overall, model (3)-(4) seems to account approximately for the basic angular thresholds and pattern orientation observed in our experiments. The model is relatively crude and one can think of a number of limitations that may explain the lack of numerical precision. Beyond the limited accuracy of the SRIM simulations employed, and the physical and mathematical approximations made in the derivation of the analytical expressions employed for the $C_{11,22}^{\mathrm{sputt,CV,impl}}$ coefficients, we can note two conspicuous simplifications that are possibly limiting the predictive accuracy of (3)-(4): *First*, the neglect of silicide formation. To date, the theoretical description of the interplay between this process and IBS nanopattering is somewhat less developed than for the mechanisms already taken into account. We can underscore the theoretical work in [13]. There, it is shown that, assuming that matter transport at the surface is controlled by mass redistribution, the contribution of silicide formation to the height equation of motion takes a similar structure to the mass currents that already occur in the absence of impurities. Indeed, now the impurity and silicide concentration fields have non-trivial behaviors, but the linear morphological analysis does not lead one to expect fundamentally different behaviors as compared with our present modeling. Quantitative changes are indeed to be expected once silicide formation is taken into account in detail, that may explain the discrepancies between our present experimental and model results.

A *second* source of inaccuracies in the predicted value for the critical incidence angle may be the approximation by which mass redistribution is considered to occur strictly at the free target surface. Currently, IBS of semiconductors is known to induce residual stress across a full amorphized layer whose thickness is of the order of the implantation range [2]. The non-trivial space variation of such a stress distribution has been shown [4] to be responsible for values of the critical angle which differ from the 45° value universally predicted by the original CV effect [35, 36, 37], at low ion energies. A similar conclusion is reached via a more microscopic analysis based on improved binary collision simulations [40]. In our present case, the substantial change in the value of the critical angle down to values smaller than 30° for 20 keV irradiation [see figure 3c] can not be accounted for by a surface-confined CV effect (SRIM simulations, not shown); we would expect it to be, rather, accounted for by this type of near-surface properties.

In the absence of further detailed information (including which is the specific silicide at play in our system and properties of the residual stress distribution), we consider the numerical results of this section as informative estimates, that in particular underscore the relevance of mass redistribution, at least for the basic patterning properties of our experimental system.

3.2. Bug-like structures

Among the different patterned morphologies observed in Figure 1 we next focus on those formed close to the threshold angle, namely at 40°, consisting of bug structures randomly scattered on a slightly rippled background. Incidentally, note that the form of such localized structures differs strongly from a sinusoidal shape, hence they remain well beyond description through a linear continuum model like equation (3). Specifically, in this section we study experimentally how this morphology forms and in which sequence, that is, whether it is the background ripples or the bugs which appear first, and how they evolve with ion fluence. Therefore, we have performed Fe^+ ion irradiation experiments at 40 keV and $\vartheta = 40°$, for ion fluence from 10^{17} up to 10^{18} ions/cm^2.

Figure 5 displays the characteristic morphologies obtained for three increasing fluence values. At the lowest ion fluences, the surface basically remains flat and featureless, but isolated hole structures appear scattered over the surface, most of them displaying a protruding rim perimeter.

The bottom inset of the 10^{17} ions/cm^2 image shows four holes of different sizes; the one on the right is rather shallow, while the hole at the center of the inset is well formed. The top inset in the same panel shows the one-dimensional (1D) profiles of these holes. With increasing hole size, the hole profile becomes asymmetric since the wall closest to the ion source presents a constant, small slope (around 6°) whereas the opposite wall increases its slope with increasing ion fluence. The graph shows the scaled ion-beam direction; note the different scales in the horizontal and vertical axes. Clearly, none of the slopes is related to the incoming beam as their values are considerably smaller than the ion incidence angle. For increasing fluence, more hole structures appear while the background surface remains flat and featureless (not shown). However, at 5×10^{17} ions/cm^2 a noticeable change occurs. First, bug-like structures have developed with an asymmetric shape whose large axis is perpendicular to the incoming ion beam. Second, the background surface is no longer featureless; instead, a ripple morphology now runs perpendicular to the ion-beam direction. These ripples have an amplitude in the $2 - 4.5$ nm range and a wavelength $\lambda \simeq 320$ nm. For the largest ion fluence employed, a similar behavior is found. Now the bug structures have become more complex with a sort of ripple structure superimposed along the ion-beam direction. Likewise, a background ripple morphology is observed with amplitudes in the $3 - 10$ nm range and typical wavelength $\lambda \simeq 390$ nm. It is worth mentioning that after 5×10^{17}ions/cm^2, no more wholes as those shown in Fig. 6(top) are found.

As mentioned above, Fe ions are known to react with the target Si atoms yielding iron silicide, which has a lower sputtering yield than Si itself leading to protruded structures. We have checked by XPS the existence of silicide. The characteristic spectra are shown in Figure 6 for the Fe2p and Si2p peaks. The main plot of the figure displays the Fe2p core level spectra of the irradiated sample and a reference Fe thin film, previously cleaned with an Ar^+ beam. One can note the change of the line shape of the peak from asymmetric, for pure Fe, to more symmetric for the irradiated

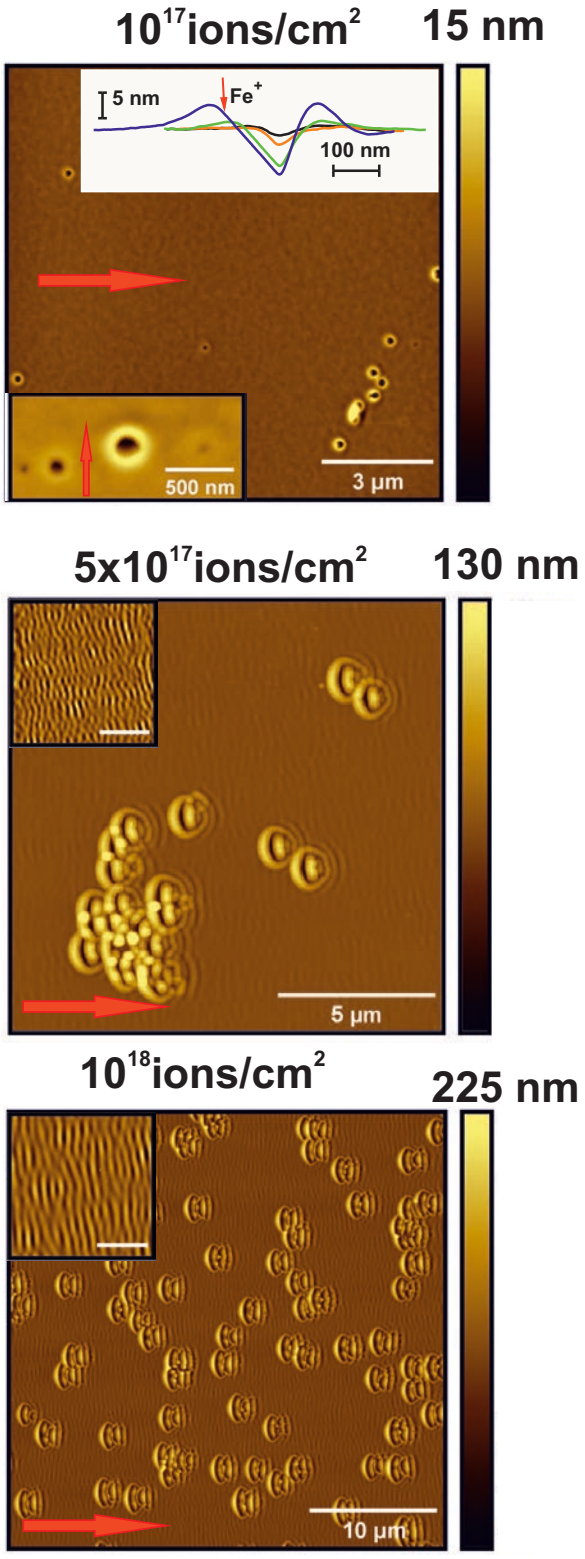

Figure 5. Characteristic morphologies induced by 40 keV Fe^+ bombardment at $\vartheta = 40°$ for increasing ion fluence, as indicated. The red arrow shows the ion-beam direction. For the lowest fluence, the bottom inset shows four different hole structures with different sizes and depths, whose 1D profiles are shown in the top inset. The insets of the two largest ion fluence images correspond to the rippled background structure. The scale bars represent 2 μm.

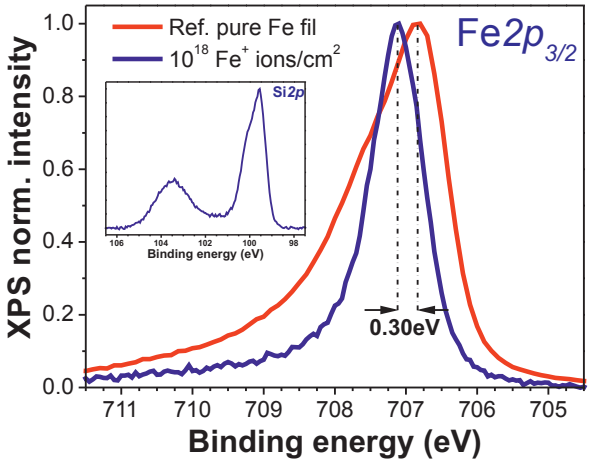

Figure 6. XPS spectrum of the Fe2p3/2 core-level for the 40 keV Fe^+ irradiated Si(100) surface at 10^{18} ions/cm^2 fluence. The spectrum (blue solid curve) is compared with that of pure Fe (red solid curve) that had been previously cleaned with an Ar^+ beam to remove surface oxidation as unambiguous fingerprint of metal-metal bonds. Inset: XPS of the Si2p core level of the same sample.

sample. This is a clear indication of the formation of an iron silicide [41, 42]. Also the main peak shifts to a larger binding energy. However, the observed shift (0.3 V) is smaller than that (0.45 V) obtained for Si targets with an adjacent Fe plate attached, irradiated on the same equipment by 40 keV Xe^+ ions [17]. The smaller shift now obtained indicates formation of a silicide with a higher Fe content [41, 42]. This is difficult to assess univocally since it is known that silicides of different stoichiometry co-exist in the Fe^+ irradiated Si targets [20].

It is unclear why there is such a transition from holes to bugs but we hypothesize that it may be related to the initial transient until the sample is uniformly implanted with Fe ion. SRIM simulations allow us to make an educated guess of the possible causes. Our experiments show that for fluences 10^{17} ions/cm^2 and 2×10^{17} ions/cm^2 only holes are present. Assuming that the target is composed only of Si, the estimated removed thickness at those fluences is approximately 47 nm and 93 nm, respectively (less than or close to the maximum ion-penetration range, which is close to 80 nm). In contrast, for fluences 5×10^{17} ions/cm^2 and 10^{18} ions/cm^2 only bugs are created and sustained. In this case, the estimated removed thickness is approximately 230 nm and 470 nm, respectively. These numbers suggest that the mechanisms of segregation/nucleation are different for low and steady Fe enrichment. The estimated parameters were obtained for Fe implantation in Si but, as we have discussed above, Fe and Si form silicides, so the numbers above are overestimates.

The confirmed presence of iron silicide prompted us to analyze the potential correlations between the iron content and the pattern morphology. Thus, we have studied the patterned samples by SEM using two different detectors sequentially, collecting secondary electrons (SE) and backscattered electrons (BS), respectively. The

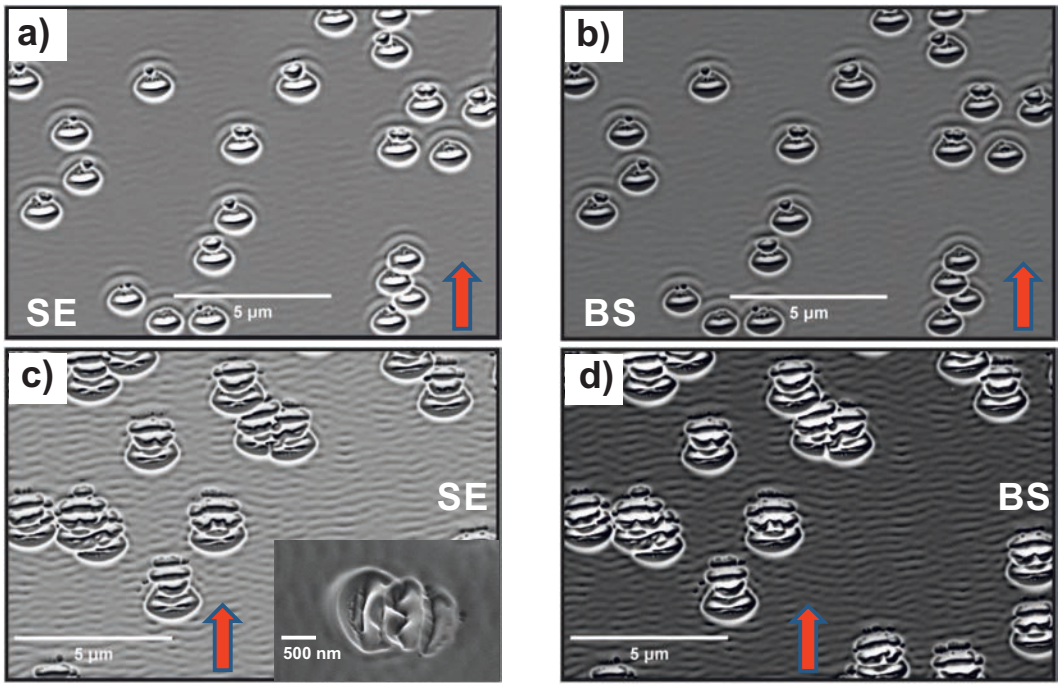

Figure 7. SEM images taken sequentially with the SE (left) and BS (right) detectors on a sample irradiated with a 5×10^{17} cm^{-2} fluence (top row) and a sample irradiated with a 10^{18} cm^{-2} fluence (bottom row). The inset in panel c) is a tilted SE image of a single bug structure. The ion-beam direction is indicated by a red arrow except for the inset, where it goes from left to right.

first detector is very sensitive to the surface morphology, yielding brighter contrast at protruding features. In contrast, the BS signal is sensitive to the atomic number of a given zone, while it has a lower spatial resolution than the SE image. Accordingly, we have analysed the two samples irradiated at higher fluence (Figure 7). At the lower fluence, there are mainly isolated structures quite similar to those seen by AFM in figure 5. It is worth noting that whereas some of them are quite rounded others start to develop a satellite structure at the location placed furthest away from the ion beam. From the comparison of the SE and BS images, it is clear that the higher metal content due to implanted Fe atoms (with higher mass) is located at the protruding regions. This space correlation is confirmed by the sample irradiated with the higher fluence (bottom row), where the structures are more developed. The inset of the SE image shows a single bug in which the sample was tilted to enhance its 3D morphology, which correlates quite well with that obtained by AFM, see below. Finally, the BS image suggests that the ridges of the background ripples are relatively Fe-rich, as they appear brighter than the ripple troughs.

Once the correlation between morphology and composition is established, we have further verified it by indirect methods with improved nanoscale resolution; namely, we perform Cs-AFM and MFM measurements in order to resolve locations with enhanced conductivity or MFM contrast. This allows us to assess the correlation between local Fe

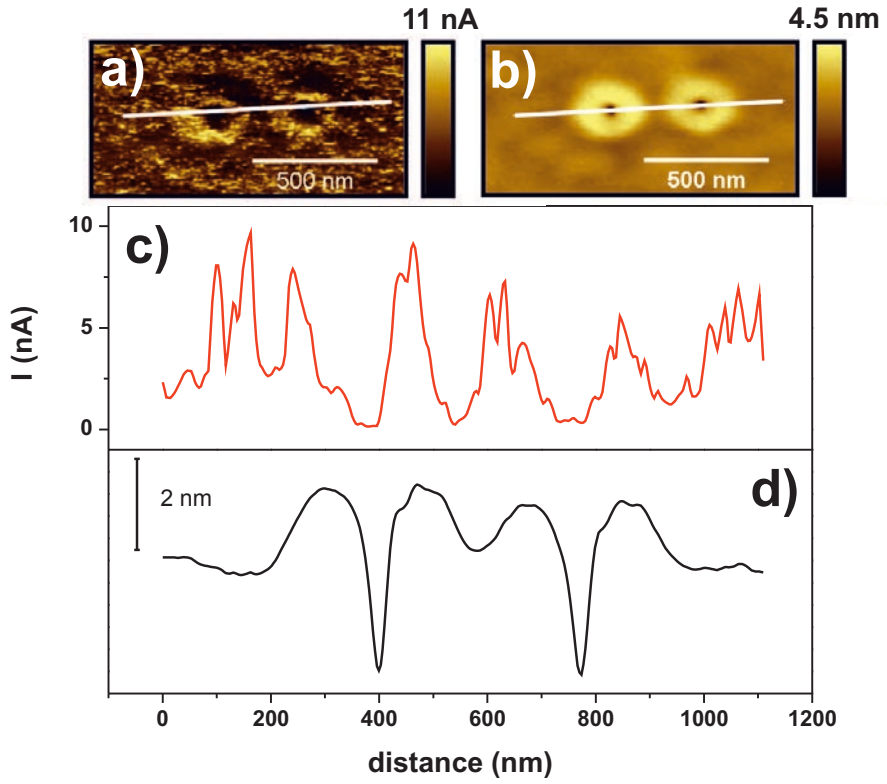

Figure 8. Top: Current (a) and topographical (b) images taken simultaneously of two holes appearing after 10^{17} ions/cm^2 Fe^+ ion bombardment. Current (c) and topographical (d) 1D profiles taken along the straight lines marked in the respective images.

content and morphology, both for the initial holes and the more developed bugs. Thus, figure 8 shows the current (Figure 8a) and topographical (figure 8b) images of two holes, around 5 nm deep, formed after an ion fluence of 10^{17} ions/cm^2. Clearly, the rim of the two holes yields an enhanced current indicating the presence of iron silicide. In contrast, the hole troughs yield a negligible current. This correlation is better appreciated in the corresponding 1D profiles shown in figures 8c and 8d. Therefore, already from the start of the patterning process, the morphological instabilities are associated with the precise space distribution of the silicide.

Figure 9 next corresponds to the sample irradiated for the highest fluence (10^{18} ions/cm^2), for which the bug structures appear scattered over a rippled background. A careful inspection of panel (a) allows us to link the most elevated topographical features of the bug structure with maxima in the corresponding current image. Likewise, surface depressions show negligible currents. Therefore, at this later stage where the structures are much larger, up to 60 nm high, the same height-current correlation exists, confirming the SEM results. Moreover, if a zoom is taken on the rippled background (Figure 9b), the maxima of the ripples are also seen to display larger currents in contrast to the ripple valleys, for which the current is practically null, as suggested by the SEM analysis in figure 7. This agrees with the findings of Khanbabaee et al. [20], namely, that the

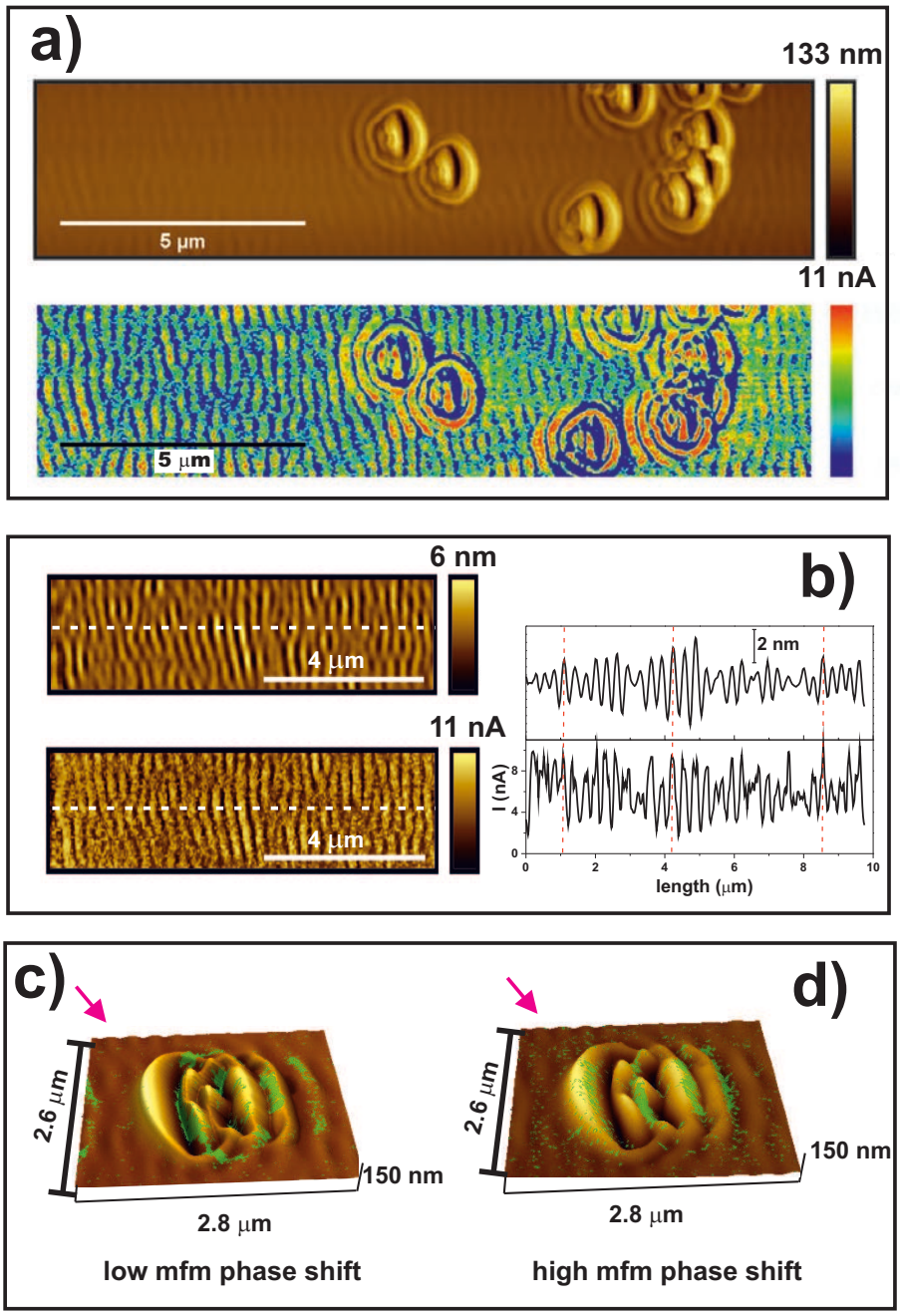

Figure 9. (a) Topographical (top) and current (bottom) images taken simultaneously on the sample irradiated with 10^{18} ions/cm^2 ion fluence. (b) Left: Topographical (top) and current (bottom) images taken simultaneously on the same rippled section of (a). The plots on the right correspond to the topographical (top) and current (bottom) 1D profiles taken along the dashed line marked on the corresponding images on the left. The dashed vertical lines correlate morphology and current maxima. Composition of the 3D topographical image of a single bug structure, with masked regions (in green) corresponding to the low (c) and high (d) values of the phase shift in the simultaneously taken MFM images.

ripple crests were Fe-rich. Finally, the MFM image taken on a single bug structure also shows different phase shifts at the protruding regions with respect to the morphological depressions, see figures 9c and 9d.

The previous analyses show that a link between morphological instabilities and rich silicide content does exist. Bug-like structures have been obtained previously [9, 43]. Although they present a different morphology, they share several features with those observed in our system: (i) they have an open-fan morphology with the longest perimeter facing the incoming Fe direction; (ii) the highest feature in the bug structure is located closest to the incoming ion beam; (iii) along the ion-beam direction, marked ripples are observed on top of the bug structures. The main difference between those systems and ours is that in our case the ion beam and the Fe supply have the same direction, as the ions are the metal impurities themselves. These similarities are important because in the previous works [9, 43] the direction of Fe supply was opposed to that of the ion beam. Thus, it seems that the roughness and the ripple structure on top of the bug and along the ion-beam direction would be determined by the ion beam, whereas the fan shape on the target plane would be defined by the Fe supply. However, Macko et al. [9] investigated different geometries for the ion beam and metal supply directions. In fact, they found that when both directions were close to each other, no pattern developed and the surface remained featureless and flat, which contrasts with our findings where the ion beam is simultaneously the metal supply source. Macko et al. [9] also proposed a tentative model to explain the bug formation and development. It is based on the development of initial surface height fluctuations under subsequent ion bombardment and metal deposition along quite different directions. Despite the differences among the various systems, the physical mechanism in our case could be similar to those relevant in [9] assuming that the height fluctuations arise from the holes observed at low ion fluences. It is important to note that the rim of these holes, which yields higher currents in the Cs-AFM images (figure 8a), is slightly higher than the surrounding regions. In our case, considering figures 5, 7, and 8, it is clear that the isolated circular holes are the initial seeds for the bug formation (figures 5 and 8a). With increasing ion fluence, new structures develop inside the hole (figures 5, 7a,b, and 8b) while their shape starts to become more asymmetric. Finally, new structures appear that tend to aggregate (figures 5, 7c,d, and 8b). Still, the origin of the initial holes remains unclear. Figure 8a suggests that the inner part has a similarly low Fe content as the flat surrounding areas. We should note that the tip size for Cs-AFM is larger than the standard one, so that the tip cannot fully enter the hole.

3.3. Analysis of the spatial distribution of bugs

Among the possible causes for hole formation, one could be the existence of Fe clusters that would become easily eroded by the ion beam, since the Fe sputtering yield is higher than those of Si and iron silicide [28]. Alternatively, holes might correspond to buried Si-rich locations in which Fe ions were not implanted, so that silicide was not formed

which made them more efficiently sputtered than the surrounding silicide regions. Other possible explanation could be the local overlap of ion impacts, which might be related with the beam parameters (divergence, rastering, etc.). Finally, the nucleation of holes could be a dynamical process where a local concentration of silicide exceeds a certain threshold giving rise to an instability. If these processes occur purely at random locations throughout the sample, one would expect the locations of the holes (and subsequently of the bugs) to be also randomly distributed. To test this hypothesis we have performed a Voronoi tessellation where each bug structure is located inside a unique (Voronoi) cell. If hole nucleation occurs at random positions, one would expect certain geometrical properties (known as Lemaitre's parameters [44]), such as the variance of the number of neighboring cells, μ_2, or the probability for a cell to have exactly 6 neighbors, p_6, to have definite, well-known values [45]. In Fig. 10 we show the Voronoi tessellation of one large SEM image corresponding to the condition of highest ion fluence. For convenience, we superimpose the Voronoi tessellation in 10(c) over the SEM micrography in panel Fig. 10(a) to illustrate the outcome of the Voronoi tessellation. Clearly, the apparent clustering of some of the experimental bug structures, Fig. 10(a), is similar to that of the randomly generated structure (with the same number of centers) shown in Fig. 10(c,d). Note also that the distributions of neighbors are similar, Figs. 10(b). Quantitatively, this apparent clustering can be tested by computing μ_2 and p_6. In particular, analyzing different parts of the same sample we find that p_6 is in the $0.281 - 0.319$ range while μ_2 is in the $1.730 - 1.931$ range; hence, both parameter values are compatible with those of a purely random pattern, with $p_6 = 0.277$ and $\mu_2 = 1.856$. This analysis supports the idea that bug nucleation is triggered by spontaneous fluctuations in the concentration of the silicide. This locally increased concentration is probably amplified by the sputtering process. Moreover, the fact that the value of p_6 is around 0.3 in all cases is a signature of a structure with low spatial order [45].

4. Conclusions

We have studied how the 40 keV Fe^+ IBS patterning of Si surfaces depends on the ion-beam incident angle. A threshold angle in the $30° - 40°$ range has been found, notably smaller than the typical values obtained for impurity-free irradiation of Si targets using noble gas ions. This threshold angle seems to increase with ion energy in the 20 to 40 keV range that we have explored. We have compared our observations with the predictions of a continuum model for impurity-free systems which contemplates the effects of an unstable sputtering yield, surface mass-redistribution, and ion implantation. The required parameters are estimated through SRIM simulations. This comparison suggests mass-redistribution as the main relaxation mechanism responsible for the existence of the critical angle, although non-negligible corrections are foreseen from the consideration of silicide formation and of a non-trivial spatial distribution for the ion-induced residual stress (equivalently, mass redistribution) within the topmost amorphized surface layer.

Experimentally, we have further studied the ripple patterns by assessing the way in

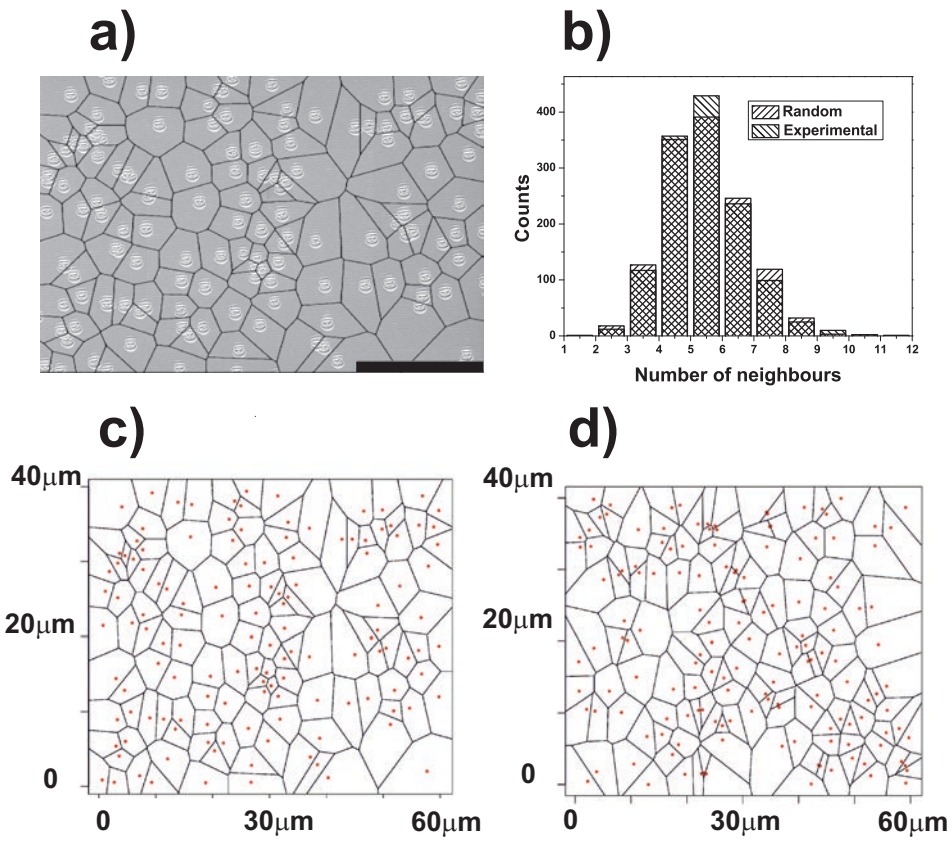

Figure 10. (a) SEM image taken with the SE detector on a sample irradiated with a 10^{18} cm^{-2} fluence displaying the surface arrangement of the induced bug structures, with its Voronoi tessellation [panel (c)] superimposed. The horizontal bar corresponds to 20 μm. (b) Histogram of number of neighbours per Voronoi cell for the tessellation obtained from a large, not shown, SEM image ($127 \times 90\,\mu$m^2) containing 1289 bug structures (shading tilted to the right) and from an equivalent image in which the structures were randomly generated (shading tilted to the left). (c) Voronoi tessellation based on the coordinates of the bugs in panel (a), which are marked in red. (d) Voronoi tessellation obtained on structures whose centres [the same total number as in panel (c)], marked in red, have been randomly generated.

which the slopes of the two faces of the induced ripples change with the ion incidence angle; we have established differences in this process with what has been reported when employing noble gas ions. We have then focused on an incidence condition (40° angle) close to threshold. Detailed morphological analysis of the fluence dependence of the process reveals that, for the 40 keV case, initially, isolated rimmed holes appear scattered on a flat, featureless surface. These structures develop with time into bug-like features, which are characterized by a more complex and rough morphology. As irradiation proceeds, a smooth ripple background eventually forms. Therefore, the formation of the localized bug-like structures seems to be independent of the ripple patterning. By means of different microscopy techniques, we have correlated the morphology with the silicide

content at the surface, from the initial up to the final stages of the nanostructuring process. In particular, we have found that the crest of the ripples and the most protruding features of the bug-like structures are richer in Fe. Similarities can be found between our bug-like structures and those previously reported for several other set-ups. A topological analysis based on Voronoi tessellation suggests that the location of the bug-like structures is purely random, making the case for spontaneous nucleation when a local concentration of Fe exceeds a certain threshold. The bugs start to appear after an initial transient whose time extent is compatible with the time required to erode a thickness comparable with the ion range, hence nucleation might be dependent on the steady state density of silicides.

Acknowledgments

This research is supported by the MINECO/FEDER (Spain/UE) grants Nos. MAT2017-85089-C2-1-R, MAT2016-80394-R, FIS2015-66020-C2-1-P, FIS2015-73337-JIN, FIS2016-78883-C2-2-P, and BIO2016-79618-R, and by Comunidad de Madrid grant NANOAVANSENS ref. S2013/MIT-3029. We want to thank C. Ballesteros and B. Galiana for their help in the SEM measurements. ARC acknowledges the Ramón y Cajal contract number RYC-2015-18047 and KL thanks FCT, Portugal, for her grant as Investigador FCT.

Appendix A

This appendix collects our results for SRIM parameter-estimates of the quantities entering the analytical expressions of the coefficients $C_{11,22}^{\mathrm{sputt,CV,impl}}$ as analytically derived in [33, 34, 35, 36, 37, 14]. At this, we closely follow the method employed and described in detail in [39]. The results are provided in table A1 and correspond to 40 keV Fe^+ irradiation of Si. Apart from these, we have additionally employed (as taken either from tables or from additional SRIM simulations) the following: sputtering yield at $\vartheta = 0°$, $Y(0) = 1.049$ atoms/ion, atomic volume for Si, $\Omega_{\mathrm{Si}} = 0.02$ nm^3, maximum of sputtering yield curve $Y(\vartheta)$ at $\vartheta_{\mathrm{max}} = 83°$, correction parameter for sputtering yield maximum [14], $\rho = 90/83 = 1.084$.

References

[1] Chan W L and Chason E 2007 *Journal of Applied Physics* **101** 121301
[2] Muñoz-García J, Vázquez L, Castro M, Gago R, Redondo-Cubero A, Moreno-Barrado A and Cuerno R 2014 *Materials Science and Engineering: R: Reports* **86** 1–44
[3] Madi C, Davidovitch B, George H, Norris S, Brenner M and Aziz M 2008 *Physical Review Letters* **101** 246102
[4] Moreno-Barrado A, Castro M, Gago R, Vázquez L, Muñoz-García J, Redondo-Cubero A, Galiana B, Ballesteros C and Cuerno R 2015 *Physical Review B* **91** 155303
[5] Engler M, Macko S, Frost F and Michely T 2014 *Physical Review B* **89** 245412
[6] Keller A, Roßbach S, Facsko S and Möller W 2008 *Nanotechnology* **19** 135303

Table A1. SRIM estimates of parameters entering coefficients $C_{11,22}^{\mathrm{sputt,CV,impl}}$ in equation (4) for 40 keV Fe^+ irradiation of Si. All quantities are mean values.

Sputtering			Implantation			CV (mass redistribution)			
Penetr. depth	Longit. straggling	Lateral straggling	Penetr. depth	Longit. straggling	Lateral straggling	Recoil depth	Vacancy depth	Knockon events	Recoil distance
a_{sputt} (nm)	α_{sputt} (nm)	β_{sputt} (nm)	a_{impl} (nm)	α_{impl} (nm)	β_{impl} (nm)	d_R (nm)	d_V (nm)	N_D (1/ion)	δ (nm/ion)
25.7	15.2	8.3	38.7	15.2	12.2	29.7	29.5	1023	204.6

[7] Sánchez-García J A, Vázquez L, Gago R, Redondo-Cubero A, Albella J M and Czigány Z 2008 *Nanotechnology* **19** 355306

[8] Macko S, Frost F, Ziberi B, Förster D F and Michely T 2010 *Nanotechnology* **21** 085301

[9] Macko S, Frost F, Engler M, Hirsch D, Höche T, Grenzer J and Michely T 2011 *New Journal of Physics* **13** 073017

[10] Zhang K, Brötzmann M and Hofsäss H 2011 *New Journal of Physics* **13** 013033

[11] Bradley R M 2011 *Physical Review B* **83** 195410

[12] Bradley R M 2012 *Physical Review B* **85** 115419

[13] Bradley R M 2013 *Physical Review B* **87** 205408

[14] Bradley R M 2016 *Journal of Applied Physics* **119** 134305

[15] Gago R, Redondo-Cubero A, Palomares F J and Vázquez L 2014 *Nanotechnology* **25** 415301

[16] Moon B, Yoo S, Kim J S, Kang S J, Muñoz-García J and Cuerno R 2016 *Physical Review B* **93** 115430

[17] Redondo-Cubero A, Gago R, Palomares F, Mücklich A, Vinnichenko M and Vázquez L 2012 *Physical Review B* **86** 085436

[18] Redondo-Cubero A, Galiana B, Lorenz K, Palomares F, Bahena D, Ballesteros C, Hernandez-Calderón I and Vázquez L 2016 *Nanotechnology* **27** 444001

[19] Mollick S A, Ghose D, Shipman P D and Bradley R M 2014 *Applied Physics Letters* **104** 043103

[20] Khanbabaee B, Lützenkirchen-Hecht D, Hübner R, Grenzer J, Facsko S and Pietsch U 2014 *Journal of Applied Physics* **116** 024301

[21] Khanbabaee B, Facsko S, Doyle S and Pietsch U 2014 *Applied Physics Letters* **105** 163101

[22] Castro M, Gago R, Vázquez L, Muñoz-García J and Cuerno R 2012 *Physical Review B* **86** 214107

[23] Zhao Y, Wang G C and Lu T M 2001 *Characterization of Amorphous and Crystalline Rough Surface: Principles and Applications* (Academic Press)

[24] Nečas D and Klapetek P 2012 *Central European Journal of Physics* **10** 181–188

[25] Pelliccione M and Lu T M 2008 *Evolution of thin film morphology: modeling and simulations* vol 108 (Heidelberg: Springer Science & Business Media)

[26] Vivo E, Nicoli M, Engler M, Michely T, Vázquez L and Cuerno R 2012 *Physical Review B* **86** 245427

[27] Hofsäss H and Zhang K 2008 *Applied Physics A* **92** 517

[28] Engler M, Frost F, Müller S, Macko S, Will M, Feder R, Spermann D, Hübner R, Facsko S and Michely T 2014 *Nanotechnolgy* **25** 115303

[29] Carter G 1999 *Journal of Applied Physics* **85** 455

[30] Garg S K, Venugopal V, Basu T, Sinha O, Rath S, Kanjilal D and Som T 2012 *Applied Surface Science* **258** 4135

[31] Garg S K, Datta D P, Kumar M, Kanjilal D and Som T 2014 *Applied Surface Science* **310** 147–153

[32] Garg S K, Datta D P, Basu T, Kanjilal D and Som T 2016 *Surface Topography: Metrology and*

Properties **4** 015002
[33] Harrison M P and Bradley R M 2014 *Physical Review B* **89** 245401
[34] Mark Bradley R and Hofsäss H 2014 *Journal of Applied Physics* **116** 234304
[35] Carter G and Vishnyakov V 1996 *Physical Review B* **54** 17647
[36] Anzenberg E, Madi C S, Aziz M J and Ludwig Jr K F 2011 *Physical Review B* **84** 214108
[37] Bobes O, Zhang K and Hofsäss H 2012 *Physical Review B* **86** 235414
[38] Ziegler J F *The Stopping and Ranges of Ions in Matter* (http://www.srim.org)
[39] Garcia M A, Rickards J, Cuerno R, Trejo-Luna R, Cañetas-Ortega J, De La Vega L R and Rodríguez-Fernández L 2017 *Physical Review Applied* **8** 064027
[40] Hofsäss H 2014 *Applied Physics A* **114** 401–422
[41] Ohtsu N, Oku M, Satoh K and Wagatsuma K 2013 *Applied Surface Science* **264** 219–224
[42] Lakshantha W J, Dhoubhadel M S, Reinert T, McDaniel F D and Rout B 2015 *Nuclear Instruments and Methods in Physics Research Section B: Beam Interactions with Materials and Atoms* **365** 114–119
[43] Zhang K, Brötzmann M and Hofsäss H 2012 *AIP Advances* **2** 032123
[44] Sadoc J F and Rivier N 2013 *Foams and emulsions* vol 354 (Springer Science & Business Media)
[45] Castro M, Cuerno R, García-Hernández M and Vázquez L 2014 *Physical Review Letters* **112** 094103